Journal of Materials Science: Materials in Electronics (2020) 31:12482–12492
https://doi.org/10.1007/s10854-020-03795-9

Phase analysis and cation distribution correlated with magnetic properties of spinel $Ba_{1-x}Sr_xFe_2O_4$ ferrites prepared at different annealing temperatures

Zein K. Heiba[1] · **Adel Maher Wahba**[2] · **Mohamed Bakr Mohamed**[1,3]

Received: 4 April 2020 / Revised: 2 June 2020 / Accepted: 11 June 2020 / Published online: 18 June 2020

Abstract

Nano $Ba_{1-x}Sr_xFe_2O_4$ samples were prepared by sol-gel autocombustion procedure. The phases developed due to different annealing temperatures and Sr-substitution amounts were determined by X'Pert HighScore Plus software. The effect of composition and annealing temperature on the lattice parameters and the crystallite size was investigated using X-ray diffraction technique. Rietveld analysis has been performed to determine the cation distribution between different crystallographic sites upon the Sr-substituted $BaFe_2O_4$ sample. Sr ion was found to prefer residing at 4a(II) site and the coordinates of this site dramatically changed with the Sr content (x). Fourier transform infrared spectrometry (FTIR) confirmed the orthorhombic structure of $BaFe_2O_4$ and the presence of the hexagonal structure ascribed to $Ba_{0.5}Sr_{0.5}Fe_2O_4$ for Sr-substituted samples. $BaFe_2O_4$ and $Ba_{0.5}Sr_{0.5}Fe_2O_4$ samples prepared at 700 °C revealed hysteresis loop with wasp-waist nature. The saturation magnetization and coercivity changed irregularly upon varying the annealing temperatures. For $Ba_{1-x}Sr_xFe_2O_4$ samples annealed at 900 °C, the saturation magnetization changed depending on the amount of Sr doping in the sample. $Ba_{0.5}Sr_{0.5}Fe_2O_4$ has the lowest coercively (424 Oe) at 700 °C annealing temperature, while its highest saturation magnetization (3.83 emu/g) is obtained at 1050°C. Many factors were considered to explain the irregular behavior of coercivity in the $Ba_{1-x}Sr_xFe_2O_4$ nano system.

1 Introduction

Ferrites materials are technologically important magnetic ceramic oxides that can be classified into spinels, garnets, hexaferrites, and orthoferrites depending on their crystal structure [1]. Spinel ferrites with the general formula of MFe_2O_4 (M=Mn, Fe, Co, Ni, Cu or Zn, etc.) can exhibit different crystal structures depending on the difference between the ionic radii of M and Fe^{3+} cations; less symmetric structures are established when the difference is large [2]. The diverse properties of the different ferrites nominated them to be used in several applications such as batteries, photodegradation, photocatalytic effect and microwave device [3–10]. As illustrative examples, $CoFe_2O_4$, $SrFe_2O_4$ and $BaFe_2O_4$ have cubic [11], hexagonal [12] and orthorhombic [13] structures, respectively. Numerous studies have been done on the phase relations in Ba–Fe–O ternary system [14]; three stable phases were reported, namely, $Ba_2Fe_2O_5$, $BaFe_2O_4$ and $BaFe_{12}O_{19}$ [15]. Barium monoferrite, $BaFe_2O_4$ is a member of spinel ferrites family that combines interesting soft magnetic properties with rather high electrical resistivities, low band gap and advantageous dielectric behavior attributed to barium-ion existence [16]. The magnetic properties of $BaFe_2O_4$ could be controlled via the substitution of Ba^{2+} and/or Fe^{3+} cations by other ions in the same manner as other ceramics materials [13, 17]. Peymanfar et al. [18] investigated the effect of annealing temperature and organic capping agent on the physical properties of nanosized $BaFe_2O_4$. They found that the organic capping agent reduced the crystallite size and subsequently improved the isotropic magnetic exchange and the microwave absorption bandwidth. The nanocomposite of $BaFe_2O_4$, annealed at 650 °C, and silicone rubber revealed substantial microwave absorption properties created from the geometrical influence of nano materials [18]. On the other hand, Dilip et al. [19] revealed that the level of barium relative to iron in $BaFe_2O_4$

✉ Mohamed Bakr Mohamed
mbm1977@yahoo.com

[1] Faculty of Science, Physics Department, Ain Shams University, Cairo, Egypt

[2] Department of Engineering Physics and Mathematics, Faculty of Engineering, Tanta University, Tanta, Egypt

[3] Physics Department, Faculty of Science, Taibah University, Al-Madinah Al-Munawara, Medina, Saudi Arabia

dramatically affects the formed phases, particle size, magnetic and dielectric properties of the system. Furthermore, $BaFe_2O_4$ indirectly prepared in the oxygen atmosphere exhibited an excellent photocatalysis effect [20].

On the other hand, $SrFe_2O_4$ is a hard ferrite with a wide range of applications in magnetic recording media and memory storage [21]. $SrFe_2O_4$ is characterized by its hexagonal structure, large magnetocrystalline anisotropy, high Curie temperature and a relatively large magnetization [22]. The effect of substitution of Sr^{2+} in different spinel ferrites was studied before by several authors [23–26]. Ateia et al. [23] reported that elastic parameters and the magnetic properties of magnesium nanoferrite were enhanced as being doped with Sr. Lima et al. [22] recorded other phases CoO, $SrCO_3$, and $SrFeO_{2.96}$ for Sr^{2+}-doped cobalt nano ferrite, attributed to the low solubility of strontium in $CoFe_2O_4$ matrix. Ahmad et al. [25] found that all magnetic parameters in single-phase $Ba_{1-x}Sr_xFe_2O_4$ prepared by sol gel auto-combustion method were enhanced upon increasing the degree of Sr-substitution. Mulyawan et al. [26] have used X-ray diffraction and Raman spectroscopy techniques to reveal that the crystal structure of $BaFe_2O_4$ prepared by solid state reaction followed by high-energy milling at 900 °C has changed from orthorhombic to a trigonal phase when doped with Sr ($Ba_{0.5}Sr_{0.5}Fe_2O_4$). Furthermore, the sample of $Ba_{0.9}Sr_{0.1}Fe_2O_4$ has exhibited the widest frequency range (11.16 GHz) for reflection loss of −38.25 dB, nominating it to be used as radar absorbing materials (RAM) [26]. The aim of the present work is to explore the structural and magnetic properties of nano $Ba_{1-x}Sr_xFe_2O_4$ ($x = 0.0, 0.1, 0.3, 0.4, 0.5$) samples prepared by sol-gel auto combustion procedure at different annealing temperatures (700, 900 and 1050 °C); new Sr content is tested at different annealing temperatures. The phases development upon annealing temperatures and Sr doping and hence their influence on the magnetic properties were inspected using Rietveld analysis for X-ray diffraction (XRD), transmission electron microscope (TEM), Fourier transform infrared spectrometry (FTIR) and vibrating sample magnetometry (VSM) techniques.

2 Experimental

Nanocrystalline Sr-doped barium $Ba_{1-x}Sr_xFe_2O_4$ (x = 0.0, 0.1, 0.3, 0.4, 0.5) monoferrite samples were prepared using sol-gel auto combustion procedure. Stoichiometric amounts of barium, strontium and iron nitrates were dissolved in small amounts of distilled water, and then mixed with anhydrous citric acid under stirring for 1 h. Meanwhile, the ammonia solution was added drop by drop to adjust the pH number from ~1 (for the acidic solution) to 7, after which the stirring process was continued for an extra 1 h. The above solution was heated on a hot plate at 100°C until the water evaporated when a dark vicious gel was obtained. Upon continuing the heating process, an ash-like powder was formed. The formed powder was grounded in an agate mortar. For samples with x = 0.0 and 0.5, the fine powder was divided into three parts and heated at 700, 900 and 1050 °C for 2 h, separately. For samples with x = 0.1, 0.3, and 0.4, the powders were sintered at 900 °C. The mechanism of the auto-combustion method used in this study can be described as following: Mixture of metal nitrates (Ba, Sr and Fe) and the organic compounds behave in a similar manner as conventional oxidants and fuels. The reaction is carried out by dissolving metal nitrates and fuel in a minimum amount of water and heating the mixture to evaporate excess water. The effect of the citric acid is to chelate the nitrate group from the metal nitrates before forming the metal oxidants Fe_2O_3, BaO, and SrO. Upon continuing the heating process, the resulting viscous liquid foams, ignites, and undergoes a self-sustained combustion, producing ashes containing the oxide product. The exothermic reaction is controlled by the fuel type and the oxidizer-to-fuel ratio. Barium or strontium carbonate could be formed as a transition phase due to the presence of C=O in the citric acid, but sintering process eliminates the carbonate phase. The phase percentage, structural and microstructural parameters were analyzed with the aid of Rietveld profile method [27] and applying MAUD [28] program for the XRD patterns recorded by Philips diffractometer (X'pert MPD). The XRD patterns were recorded using Cu-K_α radiation, 2θ range of 20 –80°, and step-scan operation mode. The instrumental broadening was corrected using LaB_6 standard sample. A Bruker Tensor 27 FTIR spectrometer with the range of 200–1000 cm^{-1} to investigate the IR spectra. The particle size and sample morphology were examined through images of HRTEM microscope (HR-TEM, Tecnai G20, FEI, Netherland) with an accelerating voltage of 200 kV. The room temperature hysteresis curves were traced from LDJ vibrating sample magnetometer (VSM, model 9600).

3 Results and discussions

3.1 Phase analysis, structural and microstructure analysis

The phases characterizing the prepared samples $Ba_{1-x}Sr_xFe_2O_4$ have been identified by applying the search-match program X'Pert HighScore Plus for XRD patterns of samples sintered at 900 °C shown in Fig. 1a. For x = 0.0 and 0.1, both samples exhibited a single orthorhombic phase with the space group $Bb2_1m$. For samples with x = 0.3 and 0.4, two phases have been identified: orthorhombic $Bb2_1m$ and hexagonal $P\ 6\ m2$. Single hexagonal phase $P\ 6\ m2$ has been identified for sample $x = 0.5$ (see Fig. 1a).

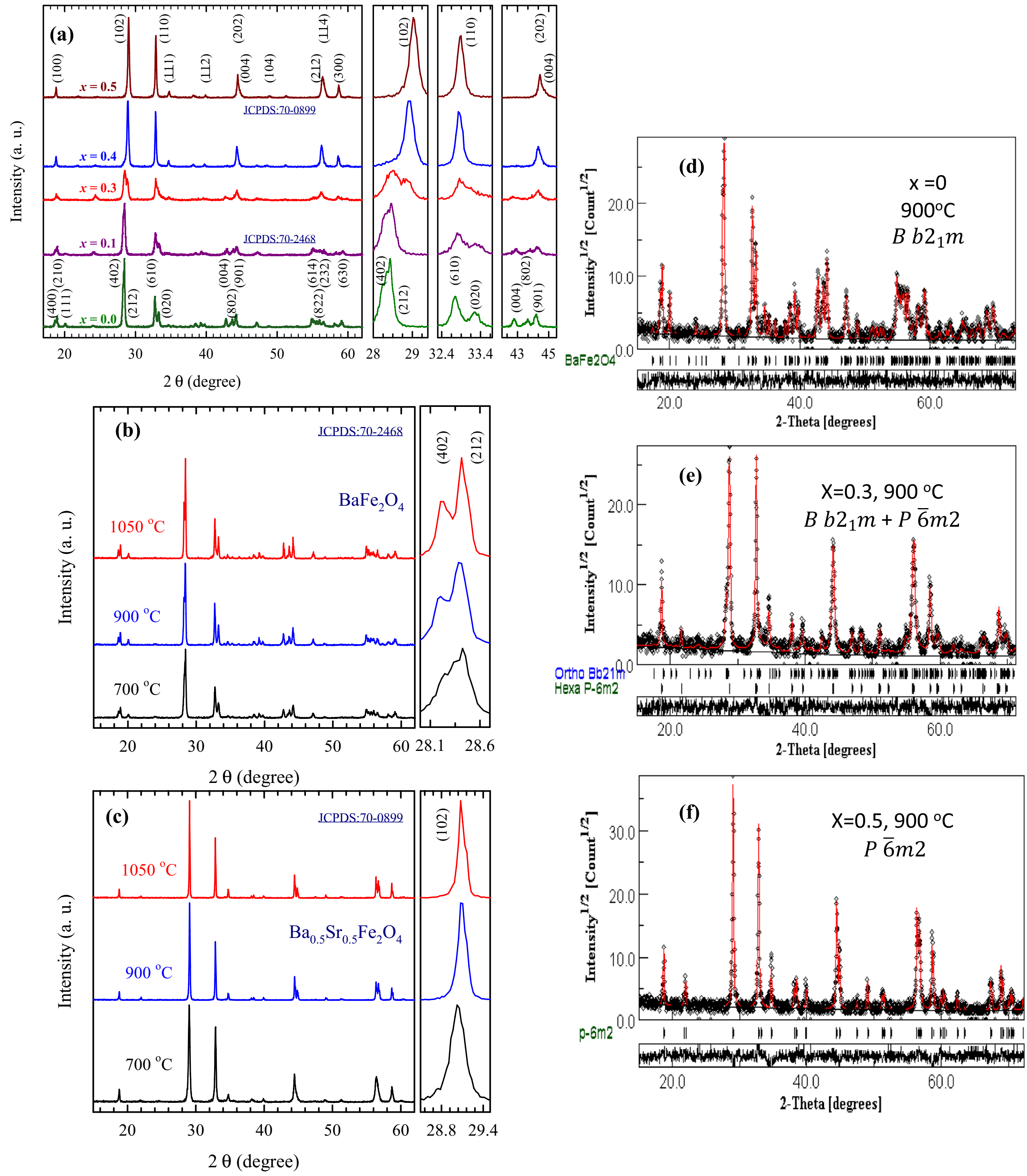

Fig. 1 X-ray diffraction patterns for: **a** $Ba_{1-x}Sr_xFe_2O_4$ ($0 \leq x \leq 0.5$), **b**, **c** $BaFe_2O_4$, and $Ba_{0.5}Sr_{0.5}Fe_2O_4$ annealed at different temperatures, Rietveld refinement for **d** $x = 0$, **e** $x = 0.3$ and **f** $x = 0.5$ samples annealed at 900 °C

Quantitative phase analysis has been performed applying Rietveld analysis; Table 1 gives the resulting structural and microstructural parameters and the percentages of phases developed, obtained from the refinement using MAUD program. Figures 1d-f illustrate the XRD patterns fitting produced from Rietveld analysis that shows explicitly the crystallographic phases of the samples. In the orthorhombic phase $Bb2_1m$, Sr incorporated into the lattice of $BaFe_2O_4$

replacing Ba ions at the site 4a, whereas in the hexagonal $P 6 m2$ phase Sr ions have its own site 1b (0 0 ½). Inspecting Table 1, interesting structural changes could be noticed. The orthorhombic phase is manifested in the samples up to x = 0.4 with a decreasing percentage from 100% for x = 0.0 and 0.1 to 3.4% for x = 0.4. For low doping x = 0.1, Sr resides in a substitutional manner for Ba keeping the orthorhombic phase $Bb2_1m$. For high doping x = 0.3 and 0.4, part of Sr substitutes Ba forming orthorhombic phase while the remaining part segregates with Ba forming the hexagonal $BaSrFe_4O_8$ phase, as illustrated schematically in Fig. 2. For x = 0.5, equivalent amounts of Sr and Ba tend to form the hexagonal $BaSrFe_4O_8$ phase. The orthorhombic lattice constants (a and b) decreased with the Sr-content (x) while the parameter (c) decreased slightly, with a pronounced decrease in the unit cell volume (Table 1). This could be attributed to the smaller ionic radius of Sr relative to that of Ba and confirms the substitutional replacement of Ba by Sr. The crystallite size of the orthorhombic phase is almost isotropic and increases slightly for x = 0.1 but clearly decreases for x = 0.3 and 0.4 which can be probably assigned to the defects introduced by Sr substitution. For the hexagonal phase, the crystallite size is anisotropic, as expected, with larger value along the c-axis.

The unit cell of orthorhombic $BaFe_2O_4$ $\left(Bb2_1m\right)$ contains 16 Fe ions, 8 Ba ions and 32 O ions. The 16 Fe ions reside at the same crystallographic site 8b but with different coordinates displaced from the averaged structure: 8 Fe(I) at $\frac{1}{24} + \Delta x_1, \frac{3}{4} + \Delta y_1, \frac{1}{4}\Delta z_1$ and 8 Fe(II) at $\frac{5}{24} + \Delta x_2, \frac{3}{4} + \Delta y_2, \frac{1}{4}\Delta z_2$. Each Fe atom is located at the center of a distorted tetrahedron of four O ions with the 16 tetrahedra forming a coordinated framework leaving cavities where tile barium atoms are accommodated. The structure is known as the 'stuffed tridymite' type [29] with a six-membered tetrahedral, forming a ring, have the conformation five-up and one-down, Fig. 2. The 8 Ba ions reside at the same crystallographic site 4a as two different kinds with different coordinates displaced from the averaged structure: 4 Ba(I) at $\frac{1}{8} + \Delta x_1, \frac{1}{4} + \Delta y_1, 0$ and 4 Ba(II) at $\frac{3}{8} + \Delta x_2, \frac{3}{4} + \Delta y_2, 0$. Ba(I) is surrounded by seven oxygen atoms while Ba(II) is surrounded by eleven oxygen atoms; such arrangement of atoms is not a close packed one. Very careful Rietveld analysis has been performed to determine the cation distribution between the crystallographic sites, specifically, the distribution of Ba ions and their replacement Sr ones. Table 2 gives the cation occupancies of Ba and Sr deduced from Rietveld analysis for x = 0.1, 0.3 and 0.4. It is obvious that Sr preferred to reside at the site 4a(II) and the coordinates of this site dramatically changed with the value of x. Figures 1b and c reveal that the crystal structure of $BaFe_2O_4$ and $Ba_{0.5}Sr_{0.5}FeO_4$ did not change with increasing the annealing temperatures. The orthorhombic and hexagonal lattice constants for $BaFe_2O_4$ and $Ba_{0.5}Sr_{0.5}FeO_4$ samples respectively are listed in Table 3, which illustrates their irregular change with the increase in the annealing temperatures. As expected, the crystallite size for both phases increases with increasing the annealing temperatures (Table 3). The structural morphology of the $BaFe_2O_4$ and $Ba_{0.5}Sr_{0.5}Fe_2O_4$ samples, both annealed at 900 °C, is investigated by the HRTEM images (Fig. 3a, b), respectively, along with their selected-area electron diffraction (SAED) patterns. HRTEM images affirm the nanosized character of both samples, and their tendency to agglomerate. The crystallite sizes demonstrated by TEM images agree quite well with those got from XRD analysis. The corresponding SAED patterns with spotty circular rings revealed a reasonable degree of crystallization of the annealed samples.

3.2 FTIR analysis

FTIR spectra of $Ba_{1-x}Sr_xFe_2O_4$ annealed at 900 °C are revealed in Fig. 4. The spectrum for $BaFe_2O_4$ sample has bands at 306, 378, 499, 624 and 773 cm^{-1} which are assigned for $BaFe_2O_4$ with orthorhombic structure [30]. As 10% of Ba is substituted with Sr, the bands shifted to higher

Table 1 Structural parameters for $Ba_{1-x}Sr_xFe_2O_4$ ($0 \le x \le 0.5$) samples annealed at 900 °C

900°							
Sr (x)	0.0	0.1	0.3		0.4		0.5
cell Para.	$Bb2_1m$	$Bb2_1m$	$Bb2_1m$ 14.9%	$P\bar{6}m2$ 85.1%	$Bb2_1m$ 3.4%	$P\bar{6}m2$ 96.6%	$P\bar{6}m2$
a (Å)	19.034	18.957	18.857	5.458	18.493	5.454	5.446
b (Å)	5.383	5.377	5.345	5.458	5.084	5.454	5.446
c (Å)	8.453	8.479	8.502	8.202	8.500	8.138	8.076
V(Å^3)	866.1	864.3	856.9	211.1	799.2	209.6	207.4
Crystallite size (nm)							
h00	121	172	98	182	38	180	365
0k0	121	145		–		–	–
001	125	165		793		882	559

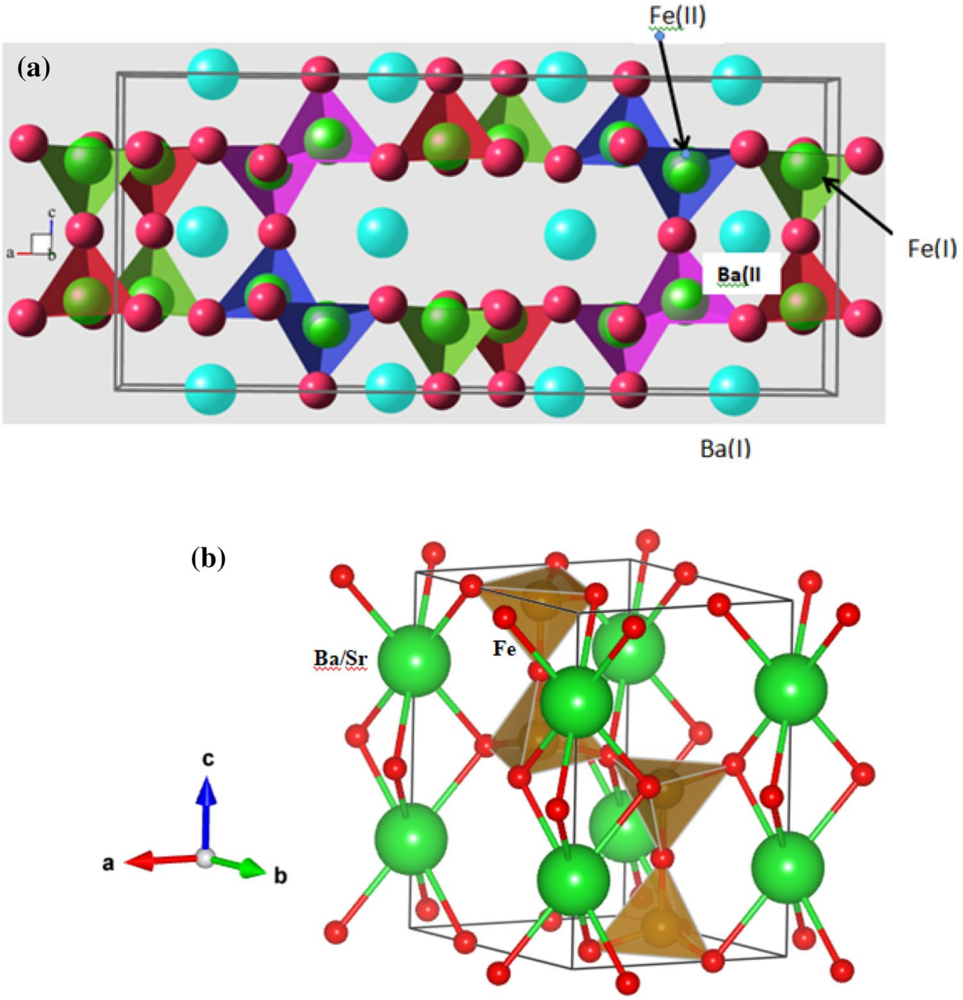

Fig. 2 Crystal structure of **a** orthorhombic $BaFe_2O_4$, and **b** hexagonal $Ba_{0.5}Sr_{0.5}Fe_2O_4$ systems

wavenumber and the intensity of the band at 624 cm^{-1} decreased, became broader, and divided into two sub-bands 615 and 648 cm^{-1}. These bands changed dramatically upon increasing Sr content for $x > 0.1$. For $x = 0.3$, an irregular shift in bands is observed, beside a significant reduction in their intensities, which is quite compatible with its low-intensity XRD pattern (Fig. 1a). Finally, the additional band appeared at 266−269 cm^{-1} for samples with $x = 0.4$ and 0.5, which could be correlated with the hexagonal structure of $SrFe_2O_4$. The bands around 605–628 cm^{-1} correspond to the intrinsic stretching vibration of the metal ion at the tetrahedral site [31, 32], while the bands at 499–512 cm^{-1} corresponded to the stretching vibration of Fe^{3+}-O^{2-} [33]. The vibration bands due to Ba–O occurred at 773–815 cm^{-1} [34]. The band at 873 cm^{-1} is assigned to the presence of Fe^{4+} cations [35]. The bands appearing at 919–926 cm^{-1} and 1078–1102 cm^{-1} are attributed to Ba–O stretching vibrations of BaO_4 units in tri-, tetra- and/or penta-borate groups [36].

3.3 Magnetic properties analysis

Figure 5b , c show the magnetic measurements at different annealing temperatures for $BaFe_2O_4$ and $Ba_{0.5}Sr_{0.5}Fe_2O_4$ samples, respectively. It can be noticed that there is no saturation in *M-H* loops for either sample at any annealing temperature, which infers the probable coexistence of a paramagnetic component with the dominating ferromagnetic phase [37]. The Wasp-Waist formation is also revealed in Fig. 5a [38] displaying the hysteresis plots for $BaFe_2O_4$ and $Ba_{0.5}Sr_{0.5}Fe_2O_4$ samples prepared at 700 °C. This type of magnetic anisotropy is called exchange anisotropy, which associated to the magnetic manifestations of an exchange

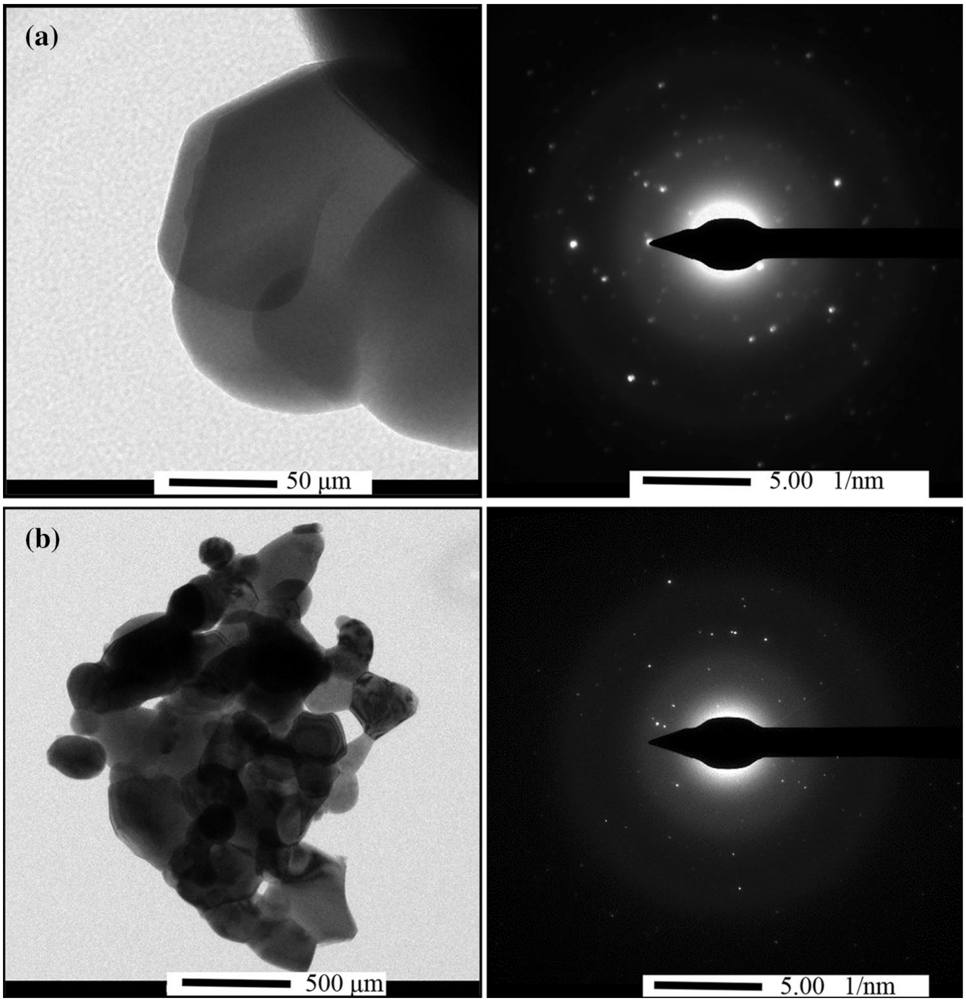

Fig. 3 TEM micrographs (left) and the corresponding SAED patterns (right) for $BaFe_2O_4$(**a**) and $Ba_{0.5}Sr_{0.5}Fe_2O_4$(**b**) samples sintered at 900 °C

Table 2 Atomic positions of Ba/Sr atoms in the different crystallographic sites of the orthorhombic phase with their occupancies in $Ba_{1-x}Sr_xFe_2O_4$ ($x = 0.1$, 0.3 and 0.4) samples annealed at 900 °C

orthorhombic $BaFe_2O_4$ ($B\ b2_1m$) at 900°								
Ba/Sr	4a(I): (u_1, v_1, 0)				4a(II): (u_2, v_2, 0)			
x	u_1	v_1	Occu		u_2	v_2	Occu	
			Ba	Sr			Ba	Sr
0.1	0.1244	0.2720	0.9906	0.0094	0.6183	0.2793	0.8094	0.1906
0.3	0.1245	0.2688	0.9758	0.0242	0.6273	0.3356	0.4242	0.5758
0.4	0.1245	0.2688	1.0	0.0	0.5255	0.0239	0.2	0.8

Table 3 Structural parameters for annealed $BaFe_2O_4$ and annealed $Ba_{0.5}Sr_{0.5}Fe_2O_4$ at different temperatures samples

	$BaFe_2O_4$ (ortho.)			$Ba_{0.5}Sr_{0.5}Fe_2O_4$ (Hexa.)		
	700 °C	900 °C	1050 °C	700 °C	900 °C	1050 °C
Lattice parameter (A)						
a	19.035	19.034	19.04	5.447	5.446	5.446
b	5.387	5.383	5.385	–	–	–
c	8.456	8.453	8.448	8.109	8.075	8.076
Crystallite size (nm)						
h00	72	121	278	81	365	336
0k0	74	125	255	–	–	–
00 l	55	121	486	295	559	539

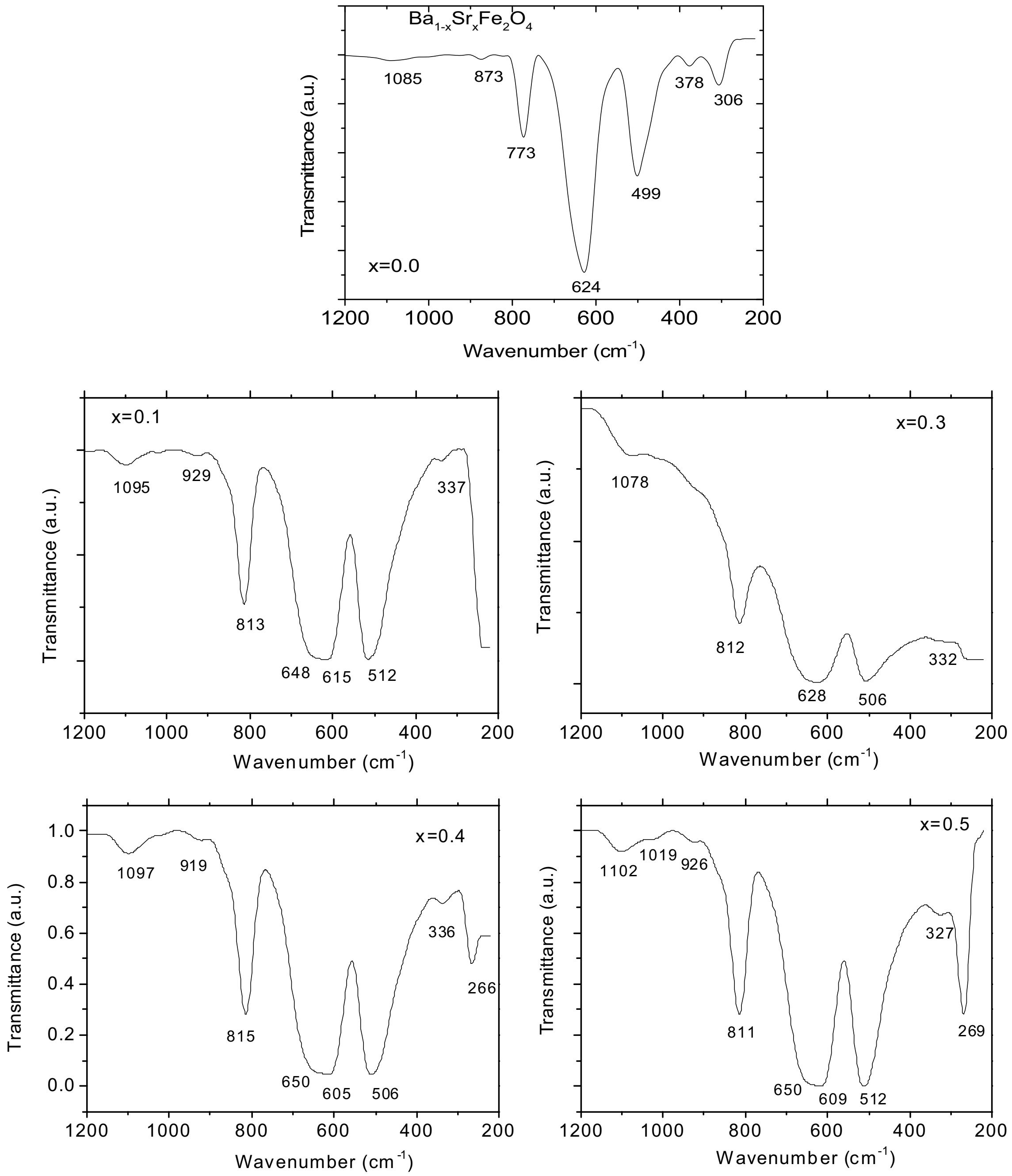

Fig. 4 FT-IR spectra for $Ba_{1\leq x}Sr_xFe_2O_4$ (0 ≤ x ≤ 0.5) samples annealed at 900 °C

coupling of magnons at the interface between two different magnetically ordered systems (ferromagnetic and non-ferromagnetic systems) [37]. Dimri et al. [39] recorded a similar behavior in $BaFe_2O_4$ synthesized by citrate combustion method at different annealing temperatures (1100–1300 °C) but the Wasp-Waist formation shape appeared at a higher temperature (1300 °C). They argued this shape into the pinning of domains and magnetocrystalline anisotropy [40].

As the sintered temperature increased a typical hysteresis loop is shown with a large coercivity for both samples (Fig. 5b , c). It is noticed from Table 4 that the coercivity (H_c) of both samples has increased from 2880 to 5832 Oe for $BaFe_2O_4$ sample and from 424.1 Oe to 6145 Oe for $Ba_{0.5}Sr_{0.5}Fe_2O_4$ sample when the annealing temperature increased from 700 to 900 °C. Upon further increase in the

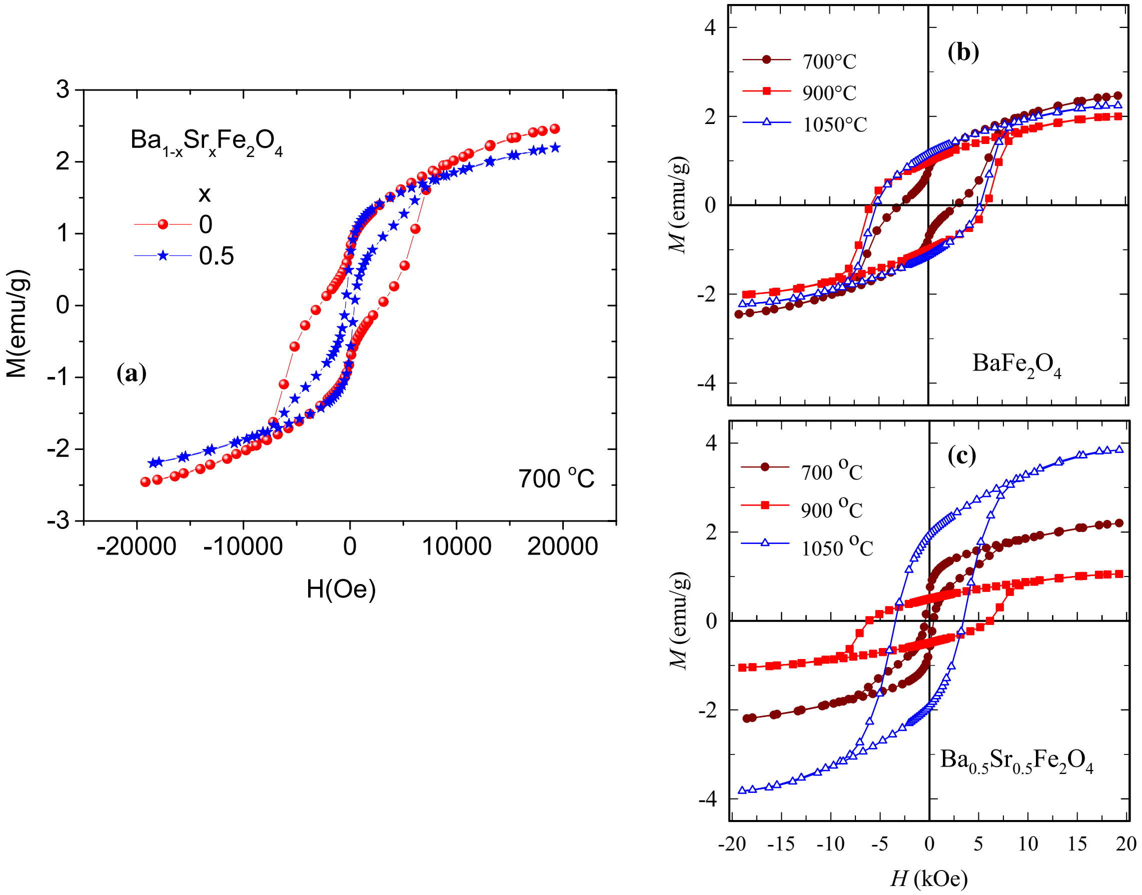

Fig. 5 Room-temperature magnetization curves for **a** $BaFe_2O_4$ and $Ba_{0.5}Sr_{0.5}Fe_2O_4$ samples annealed at 700 °C, **b** $BaFe_2O_4$ samples annealed at different temperatures and **c** $Ba_{0.5}Sr_{0.5}Fe_2O_4$ samples annealed at different temperatures

annealing temperature 1050 °C (Fig. 6), coercivity decreased to 5260 and 3438 Oe for $BaFe_2O_4$ and $Ba_{0.5}Sr_{0.5}Fe_2O_4$ samples, respectively. All coercivity values of $BaFe_2O_4$ samples annealed at different temperatures are much higher than those reported values (H_c=1205 Oe) for orthorhombic $BaFe_2O_4$ sample [41]. The obtained result is consistent with the result obtained by Dimri et al. [39]. The increase of the coercivity as the annealing temperature changed is due to the existence of the particles within the range of a single domain [42]. On the other hand, the decrease of coercivity with further increasing of the annealing temperature to 1050 °C, is due to the existence of the particles within multi domain range [42]. Furthermore, the saturation magnetization (M_s) was deduced by plotting M versus $1/H$ and taking the limit as H approaches ∞ [43]. With the increase of the annealing temperature from 700 to 900 °C, the values of M_s first decreased from 2.458 to 2.1967 emu/g to 2.0037 and 1.0536 emu/g for $BaFe_2O_4$ and $Ba_{0.5}Sr_{0.5}Fe_2O_4$ samples, respectively. With further increasing annealing temperature to 1050 °C, M_s increased again to 2.2347 and 3.8346 emu/g for $BaFe_2O_4$ and $Ba_{0.5}Sr_{0.5}Fe_2O_4$ samples, respectively. These changes could be mainly due to the increases in the crystallite size, and the contribution of Fe^{3+} ion site distribution. Maximum magnetization was lower as compared to the reported values for single crystals (M_s = 5.7 emu/g) of orthorhombic $BaFe_2O_4$ [41]. The recent low value can be partially attributed to the relative sublattice population [44], and the presence of small particles [45].

Figure 7 shows the VSM measurements of $Ba_{1-x}Sr_xFe_2O_4$ samples carried out at room temperature. When Ba^{2+} in $BaFe_2O_4$ is substituted by Sr^{2+} ions, there is a drastic change in the magnetic properties including saturation magnetization (M_s), remanent magnetization (M_r) and coercivity (H_c). The variation in the magnetic property of the samples is shown in Fig. 6c. As shown in the figure, M_s values of samples varied according to the Sr-doping amount in $BaFe_2O_4$ host material. The change in the value of M_s is most probably due to the difference in the cation sharing at different sites, as shown in Table 3, the data of which achieved from XRD analysis. Mulyawan et al. [26] revealed that $Ba_{1-x}Sr_xFe_2O_4$ prepared by high energy milling method exhibited irregular behavior of M_s, M_r and H_c with increased amount of Sr in the

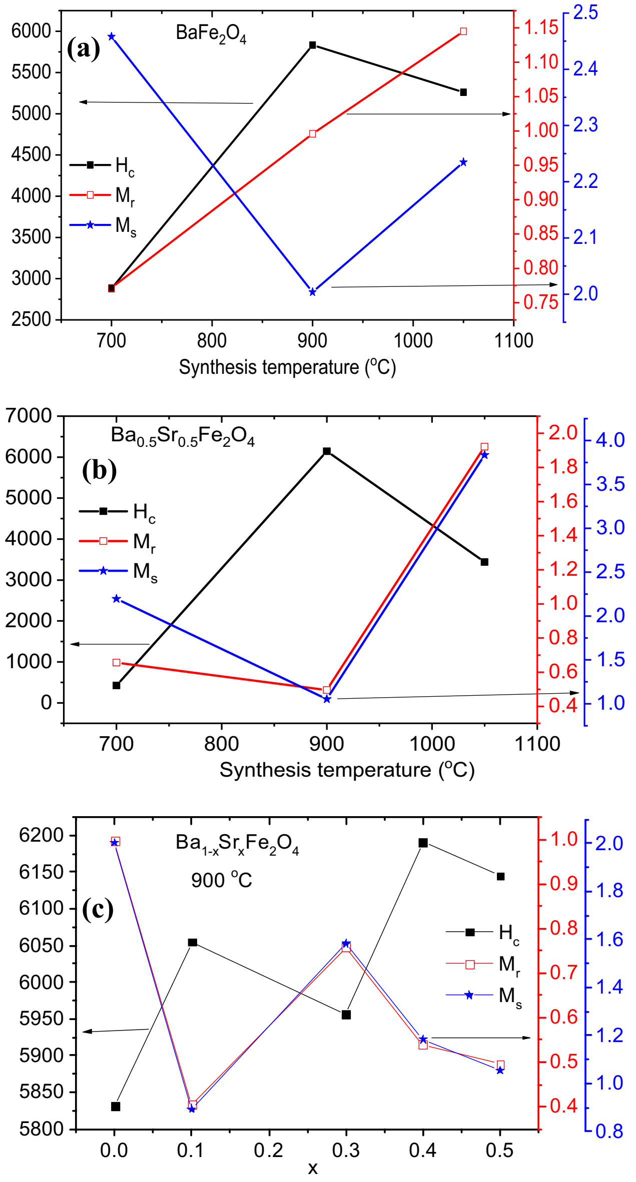

Fig. 6 Hc, Mr and Ms values for **a** annealed $BaFe_2O_4$ at different temperatures, **b** annealed $Ba_{0.5}Sr_{0.5}Fe_2O_4$ at different temperatures and **c** $Ba_{1-x}Sr_xFe_2O_4$ ($0 \leq x \leq 0.5$) samples annealed at 900 °C

Table 4 Magnetic parameters deduced from hysteresis loops for $Ba_{1-x}Sr_xFe_2O_4$ samples (x = 0.0 and 0.5 annealed at 700, 900, and 1050 °C) and (x = 0.1, 0.3 and 0.4 annealed at 900 °C)

Annealing temperture	Sample	M_s (emu/g)	H_c (Oe)	M_r (emu/g)
700 °C	$BaFe_2O_4$	2.46	2880	0.77
900 °C		2.0	5832	0.99
1050 °C		2.23	5260	1.14
900 °C	$Ba_{0.9}Sr_{0.1}Fe_2O_4$	0.89	6055	0.40
	$Ba_{0.7}Sr_{0.3}Fe_2O_4$	1.58	5957	0.76
	$Ba_{0.6}Sr_{0.4}Fe_2O_4$	1.18	6190	0.54
700 °C	$Ba_{0.5}Sr_{0.5}Fe_2O_4$	2.20	424	0.66
900 °C		1.05	6145	0.49
1050 °C		3.83	3438	1.92

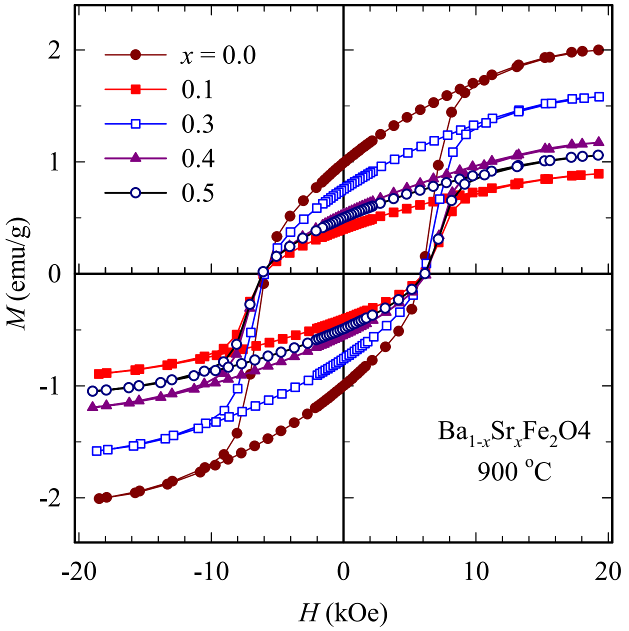

Fig. 7 Room-temperature magnetization curves for $Ba_{1-x}Sr_xFe_2O_4$ ($0 \leq x \leq 0.5$) samples annealed at 900 °C.

system. This indicates that the Sr^{2+} cation, which replacing the Ba^{2+} site in the orthorhombic structure, play an important role to originate the magnetic anisotropy and influences the domain growth and finally improved the coercivity value [26]. Upon Ba-Sr substitution of $BaFe_2O_4$ structure with small levels (x = 0.1), Sr^{2+} entered the $BaFe_2O_4$ system with orthorhombic structure and changed its H_c value. With further substitution, a new phase has been formed beside the original one, as indicated by XRD analysis. These two factors (the involvement of Sr^{2+} into the orthorhombic $BaFe_2O_4$ matrix and the formation of the second phase with hexagonal structure) compete with the crystallite size variation upon Sr-doping (Table 1 , 2), and control the irregular behavior of H_c.

4 Conclusion

Samples with x = 0.0 and 0.1 in $Ba_{1-x}Sr_xFe_2O_4$ resemble a single orthorhombic phase and samples with x = 0.3 and 0.4 exhibit orthorhombic and hexagonal phases. A single hexagonal phase is exhibited by a sample with x = 0.5. The orthorhombic lattice constants (a and b) decreased with increasing Sr-content while the parameter (c) decreased slightly. The crystallite size of the orthorhombic phase is almost isotropic and increased slightly for $x = 0.1$ but clearly decreased for $x = 0.3$ and 0.4. For the hexagonal phase at $x = 0.5$, the crystallite size is anisotropic, with larger growth along the *c*-axis. Sr ion was found to prefer residing at 4a(II) site and the coordinates of this site dramatically varied with the value of x. The crystal structure of $BaFe_2O_4$ and $Ba_{0.5}Sr_{0.5}FeO_4$ samples revealed no change with increasing the annealing temperature. HRTEM images affirmed the nanosized character for both samples. FTIR spectra confirmed the presence of the orthorhombic phase only in the samples with $x \leq 0.1$. $BaFe_2O_4$ and $Ba_{0.5}Sr_{0.5}Fe_2O_4$ samples annealed at 700 °C revealed hysteresis loops with Wasp-Waist behavior due to the exchange coupling of magnons at the interface. As the sintering temperature increased, a typical hysteresis loop for both samples are exhibited and their coercivity values first increased then decreased with further raising of annealing temperatures, being dependent on the sample crystallite size. The behavior of the saturation magnetization of the annealed samples depended on the crystallite size and Fe^{3+} distribution. Finally, the change in saturation magnetization and coercivity in $Ba_{1-x}Sr_xFe_2O_4$ was correlated with the presence of one or two phases in the matrix, crystallite size and the phase in which Sr replaces Ba (orthorhombic or/and hexagonal).

References

1. Modern Ferrite Technology, A. Goldman, Springer; 2nd edition (November 30, 2005)
2. E.C. Snelling, Soft Ferrites, Butterworths, London, 2nd Edition (1988)
3. S.M. Peymani-Motlagh, A. Sobhani-Nasab, M. Rostami, H. Sobati, M. Eghbali-Arani, M. Fasihi-Ramandi, M.R. Ganjali, M. Rahimi-Nasrabadi, Assessing the magnetic, cytotoxic and photocatalytic influence of incorporating Yb^{3+} or Pr^{3+} ions in cobalt–nickel ferrite. J. Mater. Sci.: Mater. Electron. **30**, 6902 (2019). https://doi.org/10.1007/s10854-019-01005-9
4. S.M. P-Motlagh, N. Moeinian, M. Rostami et al., "Effect of Gd^{3+}-, Pr^{3+}- or Sm^{3+}-substituted cobalt–zinc ferrite on photodegradation of methyl orange and cytotoxicity tests". J. Rare Earths **37**, 1288 (2019). https://doi.org/10.1016/j.jre.2019.04.010
5. S.M. F.Gandomi, M.Rostami Peymani-Motlagh et al., ,"Simple synthesis and characterization of $Li_{0.5}Fe_{2.5}O_4$, $LiMg_{0.5}Fe_2O_4$ and $LiNi_{0.5}Fe_2O_4$, and investigation of their photocatalytic and anticancer properties on hela cells line". J. Mater. Sci.: Mater. Electron. **30**(22), 19691 (2019). https://doi.org/10.1007/s10854-019-02320-x
6. Z.K. Heiba, M.M.S. Sanad, M.B. Mohamed, Influence of Mg-deficiency on the functional properties of magnesium ferrite anode material. Solid State Ionics **341**, 115042 (2019). https://doi.org/10.1016/j.ssi.2019.115042
7. Z.K. Heiba, M.B. Mohamed, "Effect of magnesium deficiency on magnetic properties tuning and cation redistributions of magnesium ferrite nanoparticles". J. Mater. Sci.: Mater. Electron. **30**(1), 786 (2019). https://doi.org/10.1007/s10854-018-0348-7
8. MB Mohamed, AM Wahba, ZK Heiba, "Effect of Zn Substitution on Structural, Magnetic, and Electric Properties of Ni1 − xZnxFe1.78Al0.2Gd0.02*O*4 Nanoparticles", Journal of Superconductivity and Novel Magnetism 28 (12) (2015)3675, https://doi.org/10.1007/s10948-015-3208-1.
9. S.M. Peymani-Motlagh, A. Sobhani-Nasab, M. Rostami et al., "Assessing the magnetic, cytotoxic and photocatalytic influence of incorporating Yb^{3+} or Pr^{3+} ions in cobalt–nickel ferrite". J. Mater. Sci.: Mater. Electron. **30**, 6902 (2019). https://doi.org/10.1007/s10854-019-01005-9
10. M. Rahimi-Nasrabadi, M. Rostami, F. Ahmadi et al., "Synthesis and characterization of $ZnFe_{2-x}Yb_xO_4$–graphene nanocomposites by sol–gel method". J. Mater. Sci.: Mater. Electron. **27**, 11940 (2016). https://doi.org/10.1007/s10854-016-5340-5
11. M. Rajendran, R. Pullar, A. Bhattacharya, D. Das, S. Chintalapudi, C. Majumdar, Magnetic properties of nanocrystalline $CoFe_2O_4$ powders prepared at room temperature: variation with crystallite size. J. Magn. Magn. Mater. **232**, 71 (2001). https://doi.org/10.1016/S0304-8853(01)00151-2
12. A. Mulyawan, W.A. Adi, S. Mustofa, A. Fisli, The phase transformation and crystal structure studies of strontium substituted barium monoferrite. In IOP Conference Series: Earth and Environmental Science (2017) 012070 (1–9), https://doi.org/10.1088/1755-1315/58/1/012070
13. R. Candeia, M. Souza, M. Bernardi, S. Maestrelli, I. Santos, A. Souza, E. Longo, Monoferrite $BaFe_2O_4$ applied as ceramic pigment. Ceram. Int. **33**, 521 (2007). https://doi.org/10.1016/j.ceramint.2005.10.018
14. S. Castro, M. Gayoso, A.C. Rodriguez, Study of the combustion method to prepare fine ferrite particles. J. Solid State Chem. **134**, 227 (1997). https://doi.org/10.1006/jssc.1997.7523
15. S.K. Rakshit, S.C. Parida, Z. Singh, R. Prasad, V. Venugopal, Thermodynamic properties of ternary oxides in the system Ba–Fe–O using solid-state electrochemical cells with oxide and fluoride ion conducting electrolytes. J. Solid State Chem. **177**, 1146 (2004). https://doi.org/10.1016/j.jssc.2003.10.021
16. G. Yang, B. Han, Z. Sun, L. Yan, X. Wang, Preparation and characterization of brown nanometer pigment with spinel structure. Dyes Pigments **55**, 9 (2002). https://doi.org/10.1016/S0143-7208(02)00056-6
17. Z.K. Heiba, M.B. Mohamed, A.M. Wahba, M.I. Almalowi, Effect of vanadium doping on structural and magnetic properties of defective nano-nickel ferrite. Appl. Phys. A-Mater **124**(4), 290 (2018). https://doi.org/10.1007/s00339-018-1721-3
18. R. Peymanfar, M. Rahmanisaghieh, Preparation of neat and capped BaFe2O4 nanoparticles and investigation of morphology, magnetic, and polarization effects on its microwave and optical performance. Mater. Res. Express. **5**(1–14), 105012 (2018)
19. R. Dilip, R. Jayaprakash, Effect of barium on morphological transition and magnetic and dielectric properties in ferrite nanoparticles. J. Supercond. Nov. Magn. **31**, 1741 (2018). https://doi.org/10.1007/s10948-017-4379-8
20. Y. Yang, Y. Jiang, Y. Wang, Y. Sun, L. Liu, J. Zhang, Influences of sintering atmosphere on the formation and photocatalytic property of $BaFe_2O_4$. Mater. Chem. Phys. **105**, 154 (2007). https://doi.org/10.1016/j.matchemphys.2007.04.050
21. R. Valenzuela, *Magnetic Ceramics* (Cambridge University Press, New York, 1994)
22. H.AllahB.Hamdollah Zohre Javdani, P. Salehi, Amiri, First principles calculations of optical and magnetic properties of $SrFe_2O_4$ compound under pressure. Phys. Lett. A **378**, 2644 (2014). https://doi.org/10.1016/j.physleta.2014.06.046
23. E.E. Ateia, E. Takla, A.T. Mohamed, Physical and magnetic properties of (Ba/Sr) substituted magnesium nano ferrites. Appl. Phys. A **123**, 631 (1–10 (2017). https://doi.org/10.1007/s00339-017-1246-1

24. A.C. Lima, A.P.S. Peres, J.H. Araújo, M.A. Morales, S.N. Medeiros, J.M. Soares, D.M.A. Melo, A.S. Carriço, The effect of Sr^{2+} on the structure and magnetic properties of nanocrystalline cobalt ferrite. Mater. Lett. **145**, 56 (2015). https://doi.org/10.1016/j.matlet.2015.01.066
25. M. Ahmad, J. Shaheen, W.A. Hashmi, M.N. Akhtar, M. Asif, Structural, magnetic and high frequency (1–6 GHz) parameters of Sr-substituted $BaFe_2O_4$ monoferrites synthesized by sol–gel method. Mod. Phys. Lett. B **33**(19), 1950219 (2019). https://doi.org/10.1142/S0217984919502191
26. A. Mulyawan, W.A. Adi, Yunasfi, Raman spectroscopy study, magnetic and microwave absorbing properties of modified barium strontium monoferrite $Ba_{(1-x)}Sr_{(x)}Fe_2O_4$. Mal. J. Fund. **14**(1), 73 (2018). https://doi.org/10.11113/mjfas.v14n1.750
27. J. Rodriguez-Carvajal, Recent advances in magnetic structure determination by neutron powder diffraction. Phys. B **192**, 55 (1993). https://doi.org/10.1016/0921-4526(93)90108-I
28. L. Lutterotti, Total pattern fitting for the combined size–strain–stress–texture determination in thin film diffraction. Nucl. Instrum. Methods, Phys. Res. B. **268**, 334, (2010). https://doi.org/10.1016/j.nimb.2009.09.053
29. F.P. Glasser, L.S. Dent, Glasser, Crystal Chemistry of Some AB_2O_4 Compounds. J. Am. Ceram. Soc. **46**, 377 (1963). https://doi.org/10.1111/j.1151-2916.1963.tb11755.x
30. S. Mandizadeh, M. Salavati-Niasari, M. Sadri, Hydrothermal synthesis, characterization and magnetic properties of $BaFe_2O_4$ nanostructure as a photocatalytic oxidative desulfurization of dibenzothiophene. Sep. Purif. Technol. **175**, 399 (2017). https://doi.org/10.1016/j.seppur.2016.11.071
31. S.F. Wang, X.T. Zu, G.Z. Sun, D.M. Li, C.D. He, X. Xiang, W. Liu, S.B. Han, S. Li, Highly dispersed spinel (Mg, Ca, Ba)-ferrite nanoparticles: Tuning the particle size and magnetic properties through a modified polyacrylamide gel route. Ceram. Int. **42**, 19133 (2016). https://doi.org/10.1016/j.ceramint.2016.09.075
32. H. Saravani, M.R. Esmaeilzaei, M.T. Ghahfarokhi, Synthesis and characterization of ferromagnetic $BaFe_2O_4$ nanocrystals using novel ionic precursor complex $[Fe(opd)_3]_2[Ba(CN)_8]$. J. Inorg. Organomet. Polym. 26 (, 353 (2016). https://doi.org/10.1007/s10904-016-0327-5, “,”)
33. Z.K. Heiba, A.M. Wahba, M.B. Mohamed, Structural analysis and magnetic properties of biphasic chromium-substituted copper ferrites. J. Mol. Struct. 1147 (668 (2017). https://doi.org/10.1016/j.molstruc.2017.07.003
34. T. Vijayaraghavan, S.P. Suriyaraj, R. Selvakumar, R. Venkateswaran, A. Ashok, Rapid and efficient visible light photocatalytic dye degradation using AFe_2O_4 (A = Ba, Ca and Sr) complex oxides. Mater. Sci. Eng., B 210 (43 (2016). https://doi.org/10.1016/j.mseb.2016.04.005
35. B.P. Barbero, J.A. Gamboa, and L.E. Cadús, Synthesis and characterisation of $La_{1-x}Ca_xFeO_3$ perovskite-type oxide catalysts for total oxidation of volatile organic compounds. Appl. Catal. B-Environ. **65**, 21 (2006). https://doi.org/10.1016/j.apcatb.2005.11.018
36. A. Saleem, Hussain, “Investigation of the Structure and Magnetic Properties of Co^{+2}–Ti^{+4} Substituted Barium Ferrite Powder Prepared by Sol – Gel Method. J. Phys.: Conf. Ser. **1234**, 012052 (2019). https://doi.org/10.1088/1742-6596/1234/1/012052
37. W.H. Meiklejohn, C.P. Bean, New Magnetic Anisotropy. Phys. Rev. **102**, 1413 (1956). https://doi.org/10.1103/PhysRev.102.1413
38. M.L. Tibério Alves et al., “Wasp-waisted behavior in magnetic hysteresis curves of $CoFe_2O_4$ nanopowder at a low temperature: experimental evidence and theoretical approach,” RSC Adv. (2017) https://doi.org/10.1039/C6RA28727A
39. C. Mukesh, H. Dimri, P. Khanduri, J. Agarwal, R. Pahapill, Stern, Structural, magnetic, microwave permittivity and permeability studies of barium monoferrite (BaFe2O4). J. Magn. Magn. Mater. **486**(1–6), 165278 (2019). https://doi.org/10.1016/j.jmmm.2019.165278
40. R.E. El Shater, E.H. El-Ghazzawy, M.K. El-Nimr, Study of the sintering temperature and the sintering time period effects on the structural and magnetic properties of M-type hexaferrite BaFe12O19. J. Alloys Compd. **73**, 327 (2018). https://doi.org/10.1016/j.jallcom.2017.12.228
41. A. Jaafar, S. Arekat, A. Al-Saie, M. Bououdina, Structure and magnetic properties of nanosized $BaFe_2O_4$ material. Int. J. Nanosci. **9**, 575 (2010). https://doi.org/10.1142/S0219581X10007289
42. K. El-Sayed, M.B. Mohamed, S. Hamdy, S.S. Ata-Allah, Effect of synthesis methods with different annealing temperatures on micro structure, cations distribution and magnetic properties of nano-nickel ferrite. J. Magn. Magn. Mater. **423**, 291 (2017). https://doi.org/10.1016/j.jmmm.2016.09.100
43. Z.K. Heiba, M.B. Mohamed, Structural phase analysis, optical and magnetic properties of nano Mn-doped $LiFe_5O_8$. Appl. Phys. A **124**, 818 (1–10 (2019). https://doi.org/10.1007/s00339-018-2241-x
44. V.K. Sankaranarayanan, Q.A. Pankhurst, D.P.E. Dickson, C.E. Johnson, An investigation of particle size effects in ultrafine barium ferrite. J. Magn. Magn. Mater. **125**, 199 (1993). https://doi.org/10.1016/0304-8853(93)90838-S
45. M.V. Cabanas, J.M. Gonzalez-Calbet, M.J. Vallet-Regi, Synthesis of barium hexaferrite by pyrolysis of an aerosol. J. Mater. Res. **9**, 712 (1994). https://doi.org/10.1557/JMR.1994.0712